

Manuscript version: Author's Accepted Manuscript

The version presented in WRAP is the author's accepted manuscript and may differ from the published version or Version of Record.

Persistent WRAP URL:

<http://wrap.warwick.ac.uk/132670>

How to cite:

Please refer to published version for the most recent bibliographic citation information. If a published version is known of, the repository item page linked to above, will contain details on accessing it.

Copyright and reuse:

The Warwick Research Archive Portal (WRAP) makes this work by researchers of the University of Warwick available open access under the following conditions.

Copyright © and all moral rights to the version of the paper presented here belong to the individual author(s) and/or other copyright owners. To the extent reasonable and practicable the material made available in WRAP has been checked for eligibility before being made available.

Copies of full items can be used for personal research or study, educational, or not-for-profit purposes without prior permission or charge. Provided that the authors, title and full bibliographic details are credited, a hyperlink and/or URL is given for the original metadata page and the content is not changed in any way.

Publisher's statement:

Please refer to the repository item page, publisher's statement section, for further information.

For more information, please contact the WRAP Team at: wrap@warwick.ac.uk.

Transparent Ferroelectric Crystals with Ultrahigh Piezoelectricity

Chaorui Qiu,^{1†} Bo Wang,^{2†} Nan Zhang,^{1†} Shujun Zhang,^{3,2} Jinfeng Liu,¹ David Walker,⁴ Yu Wang,⁵
Hao Tian,⁵ Thomas R. Shrout,² Zhuo Xu,^{1*} Long-Qing Chen^{2*} and Fei Li^{1*}

¹Electronic Materials Research Lab, Key Lab of Education Ministry/International Center for Dielectric Research, School of Electronic and Information Engineering, State Key Laboratory for Mechanical Behavior of Materials, Xi'an Jiaotong University, Xi'an, 710049, China

²Materials Research Institute, Department of Materials Science and Engineering, The Pennsylvania State University, University Park, PA, 16802, USA

³ISEM, Australian Institute for Innovative Materials, University of Wollongong, Wollongong, NSW 2500, Australia

⁴Department of Physics, University of Warwick, Coventry CV4 7AL, UK

⁵School of Physics, Harbin Institute of Technology, Harbin 150001, China

[†]These authors contributed equally

*Corresponding authors (Z.X.: xuzhuo@xjtu.edu.cn; L.Q.C.: lqc3@psu.edu; F.L.: ful5@xjtu.edu.cn)

Transparent piezoelectrics are highly desired for numerous hybrid ultrasound-optical devices ranging from photoacoustic imaging transducers to transparent actuators for haptic applications^{1,2,3,4,5,6,7}. However, it has long been challenging to simultaneously achieve high piezoelectricity and perfect transparency, since most high-performance piezoelectrics are ferroelectrics that contain high-density light-scattering domain walls. Here, through a combination of phase-field simulations and experiments, we demonstrate a relatively simple method of using an *AC* electric-field to engineer the domain structures of originally opaque rhombohedral $\text{Pb}(\text{Mg}_{1/3}\text{Nb}_{2/3})\text{O}_3$ - PbTiO_3 (PMN-PT) crystals to simultaneously generate near-perfect transparency, ultrahigh piezoelectric coefficient d_{33} (>2100 pC N⁻¹), outstanding electromechanical coupling factor k_{33} ($\sim 94\%$), and large electro-optical coefficient γ_{33} (~ 220 pm V⁻¹), far beyond the performance of the commonly used transparent ferroelectric crystal LiNbO_3 ($d_{33} \sim 40$ pC N⁻¹, $k_{33} \sim 47\%$, and $\gamma_{33} \sim 30$ pm V⁻¹). We find that increasing the domain sizes leads to a higher value of d_{33} for the [001]-oriented rhombohedral PMN-PT crystals, challenging the conventional wisdom that decreasing the domain sizes always results in higher piezoelectricity^{8,9,10}. This work presents a paradigm to achieve an unprecedented combination of properties and functionalities through ferroelectric domain engineering, and the new transparent ferroelectric crystals reported here are expected to open up a wide range of hybrid device applications, such as medical imaging, self-energy-harvesting touch screens and invisible robotic devices.

Achieving simultaneous high piezoelectricity and perfect transparency in a piezoelectric material has long been a great challenge. For example, traditional high-performance piezoelectric transducers are typically made from perovskite ferroelectric ceramics and crystals with chemical compositions around their morphotropic phase boundaries (MPBs), e.g., $\text{Pb}(\text{Zr,Ti})\text{O}_3$ (PZT) ceramics and domain-engineered $\text{Pb}(\text{Mg}_{1/3}\text{Nb}_{2/3})\text{O}_3$ - PbTiO_3 (PMN-PT) crystals. These materials possess very high d_{33} and k_{33} ^{11,12,13,14}, but they are usually opaque in the visible light spectrum. On the other hand, the commonly used transparent piezoelectrics, LiNbO_3 crystals and polyvinylidene fluoride (PVDF) polymers^{6,7}, have good transparency but much lower values of d_{33} and k_{33} (LiNbO_3 : $d_{33} < 40 \text{ pC N}^{-1}$, $k_{33} \sim 47\%$; PVDF: $d_{33} \sim 20 \text{ pC N}^{-1}$, $k_{33} \sim 16\%$), which severely limit the acoustic source level, bandwidth, and sensitivity of the transparent transducers.

In addition to the extrinsic effects, such as porosity and grain boundaries which exist ubiquitously in ceramics, the poor transparency in PZT ceramics and domain-engineered PMN-PT crystals is closely associated with the light scattering and reflection by their ferroelectric domain walls. One can think of two possible approaches to reduce the light-scattering domain walls. The first is to pole a ferroelectric crystal along the polar direction to achieve a single-domain state. However, the value of d_{33} for such single-domain PMN-PT crystals is generally very low,^{13,14} much below that of [001] poled multi-domain rhombohedral PMN-PT crystals ($> 1500 \text{ pC N}^{-1}$). In principle, one can first pole a rhombohedral PMN-PT crystal along the [111] direction to achieve a single domain state with good transparency, then rotate the crystal to [001] direction to guarantee the high longitudinal piezoelectricity. However, this approach is not feasible in practice as detailed in the [Methods section](#). The second approach is to dramatically reduce the domain sizes by breaking the domains into polar nanoregions whose spatial sizes (a few to tens of nanometres) are much smaller than the wavelength of visible light, thus greatly improving the light transparency as observed in La-doped PZT^{15,16}. However, improving the transparency using polar nanoregions was achieved at the expense of a drastically reduced remanent polarization and thus very low values of d_{33} . Therefore, optical functionalities in high-performance piezoelectrics have not been realized despite more than 50 years of efforts.

In this work, we show that one can use *AC* electric-fields to effectively eliminate light-scattering 71° domain walls for [001]-oriented rhombohedral PMN-PT crystals to achieve both near-perfect transparency and ultrahigh piezoelectricity. We first perform phase-field simulations to study the domain evolution of a [001]-oriented 0.72 $\text{Pb}(\text{Mg}_{1/3}\text{Nb}_{2/3})\text{O}_3$ -0.28 PbTiO_3 (PMN-28PT) rhombohedral crystal using both conventional *DC* and *AC* electric-fields. We generate the initial pristine unpoled state starting from a random distribution of small polarizations representing a high-temperature paraelectric state. The obtained multi-domain state contains all eight possible $\langle 111 \rangle$ rhombohedral domain variants with an average size of $\sim 20 \text{ nm}$. Three types of domain walls are present in the unpoled rhombohedral crystal, i.e., 71°, 109° and 180° domain walls.

Under a *DC* electric-field along the [001] direction, the four domain variants with polarizations along $[11\bar{1}]$, $[\bar{1}1\bar{1}]$, $[\bar{1}\bar{1}1]$ or $[1\bar{1}\bar{1}]$ are switched to the $[111]$, $[1\bar{1}1]$, $[\bar{1}\bar{1}1]$ or $[\bar{1}11]$ directions. Thus, only 71° and 109° domain walls survived while the 180° domain walls were eliminated by poling, as

75 shown **Fig. 1a**. The horizontal layers are separated by a set of 109° domain walls parallel to the (001)
76 plane, while within each lamina, there are 71° domain walls approximately parallel to $\{011\}$ planes. It
77 should be noted that 71° domain walls can scatter light since the refractive indices n_o and n_e (the
78 subscript letters ‘o’ and ‘e’ represent ordinary and extraordinary light, respectively) change as light
79 travels across a 71° domain wall, as shown in Extended Data Fig. 1. In contrast, 109° domain walls do
80 not induce light scattering since the refractive indices are the same for the domains on both sides of a
81 109° domain wall.

82 Our phase-field simulations demonstrate that the application of an *AC* electric-field effectively reduces
83 the number of 71° domain walls with only two 71° domain walls left in each lamina after *AC*-poling,
84 leading to the much larger domain size within each lamina. To understand the reason for the
85 elimination of 71° domain walls by *AC*-poling, we analyse the domain evolution during the
86 polarization reversal process, as shown in Fig. 1b and SI **Videos** 1&2. One can see that the reversal of
87 electric field causes the “swinging” of 71° domain walls, i.e., 71° domain walls alternating between
88 (011) and (01 $\bar{1}$) planes. During this process, the contiguous 71° domains tend to merge with each other,
89 and thus a significant increase in 71° domain size after *AC*-poling. In addition, as presented in Extended
90 Data Fig. 2, the total free energy of the system is reduced during *AC*-poling since the energies arising
91 from the discontinuities of polarization/strain associated with domain walls decrease as the domain
92 wall density decreases. In other words, alternating the polarity of the electric-field back and forth
93 lowers the free energy of a ferroelectric crystal, leading to a domain structure with reduced domain
94 wall density. As discussed above, due to the significantly decreased 71° domain wall density, the light
95 transmission of the *AC*-poled sample is expected to be superior to a corresponding *DC*-poled sample.

96 Following the phase-field simulations, we characterized the domain structures of *AC*-poled and *DC*-
97 poled PMN-28PT crystals. Using birefringence imaging microscopy (BIM)¹⁷, we characterized the
98 orientation (ϕ) of the principal axis of the optical indicatrix projected on the (001) planes, as shown in
99 **Fig. 2a**. For a rhombohedral single domain, the projection of the optical axis is along the face diagonal.
100 Therefore, the orientation ϕ of a rhombohedral domain would be 45° or 135° , which are represented by
101 blue and red colours respectively, as shown by the colour bar in Fig. 2a. A multi-domain crystal may
102 show two or more colours simultaneously in the projection map due to the overlap of ferroelectric
103 domains and domain walls along the light propagation path.

104 For the unpoled sample, the orientation map shows an irregular colour distribution on a very fine scale.
105 This is because the domain size of the as-grown PMN-PT is much smaller than the experimental
106 resolution (i.e., the wavelength of the light: 590 nm); therefore, the exact domain pattern may not be
107 clearly revealed. Compared to classical ferroelectrics (e.g., BaTiO₃), the relatively small domain size in
108 relaxor ferroelectrics (on the order of several tens of nanometres before poling^{18,19,20}) is attributed to
109 the presence of random fields/bonds that inhibits the growth of ferroelectric domains^{21,22,23,24}.

110 After *DC*-poling, the regions with the same colour increase in size, and cross-like boundaries are
111 approximately along the [100] and [010] directions, which are associated with the projections of 71°

112 domain walls [(101), (10 $\bar{1}$), (011) or (01 $\bar{1}$) planes] on the (001) plane. In this image, the colours of
 113 most regions are neither red nor blue. Of particular importance is the significantly enlarged domain size
 114 in the *AC*-poled sample where the in-plane size of the rhombohedral domain is on the millimetre scale.
 115 It should be noted that the domain size obtained from phase-field simulation is much smaller than that
 116 from experiments. This is due to the fact that the spatial scale in the phase-field simulation (512 nm) is
 117 much smaller than that of the materials in experiments (millimeter scale). By increasing the scale in
 118 phase-field simulation, the domain size of *AC*-poled crystal is found to increase (Extended Data Fig. 3).
 119 It is difficult to perform a phase-field simulation on millimeter scale and at the same time to revolve the
 120 polarization profiles across domain walls of the thickness of ~ 1 nm. In this work, we used phase-field
 121 simulations to qualitatively analyse the domain evolution of PMN-28PT crystals during *AC*-poling. We
 122 also characterized the cross-section domain structure of *AC*-poled and *DC*-poled samples to investigate
 123 the domain size for the out-of-plane direction. As shown in Extended Data Fig. 4, we found that the
 124 width between two neighbouring 109° domain walls is similar for both samples (~ 1 micron), indicating
 125 that most 109° domain walls survived after *AC*-poling, which is consistent with phase-field simulations.

126 X-ray diffraction patterns confirm the main observations from the BIM images. Fig. 2b shows the {222}
 127 reflections for the [001]-oriented PMN-28PT crystals. In this measurement, if the rhombohedral
 128 domain variants are evenly distributed in the sample, there should be two diffraction peaks in the 2θ - ω
 129 map: one peak is associated with the (222) plane at a lower 2θ , and the other peak is associated with the
 130 remaining three {222} planes at a higher 2θ . Thus, the integrated intensity of the high- 2θ reflection is
 131 supposed to be three times that of the low- 2θ reflection. This is approximately what has been observed
 132 in the unpoled sample. The diffuse distribution of the diffraction along the ω axis is associated with the
 133 lattice distortions due to the existence of domain walls. After *DC*-poling, the diffraction peaks converge
 134 into distinctive sharper reflections, indicating that the domains become larger and the volume fraction
 135 of domain walls is decreased. Eventually, in the *AC*-poled sample, only the high- 2θ diffraction peak is
 136 observed, and the diffusiveness of the diffraction peak along the ω axis is much smaller than that of the
 137 *DC*-poled and unpoled samples (Extended Data Fig. 5). These features reveal that the X-ray beam is
 138 almost incident on a single domain of *AC*-poled sample. The size of the beam here is approximately 1
 139 mm², which leads us to believe that the in-plane domain size of the *AC*-poled sample is equal to or
 140 greater than this value.

141 Due to the unique domain structure, *AC*-poled PMN-28PT crystals exhibit numerous attractive
 142 properties in addition to their ultrahigh piezoelectricity, including a high electro-optical coefficient γ_{33}
 143 of 220 pm V⁻¹, near-perfect light transmittance, and an enhanced birefringence (Extended Data Table 1).
 144 **Fig. 3a** shows photos of the *AC*-poled and *DC*-poled samples, where *AC*-poled samples are clearly
 145 transparent. The light transmittance of *AC*-poled sample is found to be very close to its theoretical limit
 146 and is much higher than that of the *DC*-poled sample, especially for the visible light spectrum, as
 147 shown in Fig. 3b. The light with a wavelength below 400 nm is completely absorbed due to the optical
 148 absorption edge (~ 3.10 eV), which is similar to most oxygen-octahedral perovskites^{25,26}. At a
 149 wavelength above 400 nm, the light absorption coefficient of the *AC*-poled sample is found to be

almost zero, while the absorption coefficient of the *DC*-poled sample remains large and monotonically decreases with increasing wavelength (Extended Data Fig. 6).

The birefringence of the *AC*-poled crystals is approximately one order of magnitude higher than that of their *DC*-poled counterparts, as shown in Fig. 3c. This difference is associated with the different domain structures. The principle axis of the optical indicatrices of the domains on both sides of a 71° domain wall are perpendicular to each other on the (001) plane, resulting in cancellation of the birefringence as light travels through a 71° domain wall (see [Methods section for Polarized Light Microscope](#)). For *AC*-poled crystals, however, the birefringence is approximately equal to that of the intrinsic value of a single-domain rhombohedral PMN-28PT crystal due to the substantially decreased number of 71° domain walls.

In addition, the *AC*-poled crystals exhibit a 30% enhancement in d_{33} over the *DC*-poled crystals. This phenomenon was observed in many *AC*-poled relaxor-PT crystals^{27,28,29,30}. To understand the mechanism for the enhanced piezoelectricity, we conducted phase-field simulations to calculate the piezoelectricity of PMN-28PT with different 71° domain sizes, as shown in **Fig. 4a**. The variation of polar vectors around a 71° domain wall is depicted in Fig. 4b. For an ideal rhombohedral domain, the polar vectors are along $\langle 111 \rangle$ directions, and the angle between the polar vector and [011] direction is 35.3°. However, the presence of 71° domain walls causes the polar vectors to rotate towards the [011] direction to minimize the polarization gradient and elastic energies associated with the polarization/strain discontinuities around the domain walls. With decreasing domain size, the impact of the domain walls on the polarization becomes more prominent, resulting in a larger deviation of polarization from the $\langle 111 \rangle$ directions, as shown in Fig. 4c. Because of variations in polarization, the free energy profile of the system is also affected. As shown in Fig. 4d, the averaged free energy profile of the system as a function of ΔP_z is flattened with the increase in the 71° domain width, i.e., the curvature of free energy profile $(\frac{\partial^2 G}{\partial P_z^2})_{\Delta P_z=0}$ decreases with increasing 71° domain width. Thus, the calculated dielectric permittivity ϵ_{33} and d_{33} increase with enlarging 71° domain width, as shown in Figs. 4e&f.

It should be noted that the observed enhancement in piezoelectricity with increasing domain size is not universal to all ferroelectric crystals. It is expected that the piezoelectricity of ferroelectrics is also related to the symmetry of ferroelectric phase and domain configurations^{31,32}. For example, in tetragonal BaTiO₃^{8,9,10} and high-temperature-poled PZN-PT crystals³³, where domain configurations are very different from PMN-28PT, the domain-size-dependence of piezoelectricity shows an opposite trend to that we observed here.

For the purpose of practical applications, we also studied the temperature stability of properties of *AC*-poled PMN-28PT crystals (Extended Data Fig. 7), which indicates that the temperature dependent electromechanical behaviors of *AC*- and *DC*-poled samples are very similar. Of particular interest is fact that at temperatures below rhombohedral-tetragonal phase transition temperature (~95 °C), the

domain structure remains essentially the same, and no depolarization behaviour is observed, indicating AC-poled crystals can be used up to their respective phase transition temperatures.

In summary, we report a simple approach of using AC electric-fields to simultaneously achieve near-perfect transparency, enhanced piezoelectricity and birefringence for rhombohedral PMN-PT crystals. Such transparent crystals are expected to find a wide range of applications in electro-optical-mechanically coupled devices. Both experimental and simulated results demonstrate that the enhanced piezoelectricity of [001]-poled rhombohedral PMN-PT crystals through AC-poling is due to the increased domain size, in contrast to the long-standing belief that decreasing domain size always leads to higher piezoelectricity.

References

1. Wang, L.V. Multiscale photoacoustic microscopy and computed tomography. *Nat. Photonics* **3**, 503–509 (2009).
2. Chen, X. *et al.* Transparent lead lanthanum zirconate titanate (PLZT) ceramic fibers for high-frequency ultrasonic transducer applications. *Ceram. Inter.* **42**, 18554–18559 (2016).
3. Tshering, C. & Tshering D. Renewable mobile charger using piezoelectric transducer. *Res. J. Recent Sci.* **7**, 20–23 (2018)
4. Sette D. *et al.* Transparent piezoelectric transducers for large area ultrasonic actuators. *2017 IEEE 30th International Conference on Micro Electro Mechanical Systems (MEMS)*. IEEE, 793–796 (2017).
5. Modarres, A., Ramstein, C., Cruz-Hernandez, J. M., Danny, A. & Grant, A. G. Transparent composite piezoelectric combined touch sensor and haptic actuator. *U.S. Patent* 2011/0261021 A1 (2011).
6. Thalhammer, G., McDougall, C., MacDonald, M. P., & Ritsch-Marte, M. Acoustic force mapping in a hybrid acoustic-optical micromanipulation device supporting high resolution optical imaging. *Lab on a Chip* **16**, 1523-1532 (2016).
7. Niederhauser, J. J., Jaeger, M., Hejazi, M., Keppner, H. & Frenz, M. Transparent ITO coated PVDF transducer for optoacoustic depth profiling. *Opt. Commun.* **253**, 401–406 (2005).
8. Wada, S., Yako, K., Kakemoto, H., Tsurumi, T. & Kiguchi, T. Enhanced piezoelectric properties of barium titanate single crystals with different engineered-domain sizes. *J. Appl. Phys.* **98**, 014109 (2005).
9. Hlinka, J., Ondrejovic, P. & Marton, P. The piezoelectric response of nanotwinned BaTiO₃. *Nanotechnology* **20**, 105709 (2009).
10. Ahluwalia, R., Lookman, T., Saxena, A. & Cao, W. Domain-size dependence of piezoelectric properties of ferroelectrics. *Phys. Rev. B* **72**, 014112 (2005).
11. Jaffe, B., Cook, W. R., & Jaffe, H. *Piezoelectric ceramics* (Academic press, 1971).
12. Damjanovic, D. Comments on origins of enhanced piezoelectric properties in ferroelectrics. *IEEE Trans. Ultrason. Ferroelectr. Freq. Contr.* **56**, 1574–1585 (2009).
13. Sun, E. W. & Cao, W. W. Relaxor-based ferroelectric single crystals: growth, domain engineering, characterization and applications. *Prog. Mater. Sci.* **65**, 124–210 (2014).

- 225 14. Zhang, S. J. *et al.* Advantages and challenges of relaxor-PT ferroelectric crystals for
226 electroacoustic transducers- a review. *Prog. Mater. Sci.* **68**, 1–66 (2015).
- 227 15. Haertling, G. H. Ferroelectric ceramics: history and technology. *J. Am. Ceram. Soc.* **82**, 797–818
228 (1999).
- 229 16. Ruan, W. *et al.* Large electro - optic effect in La-doped $0.75\text{Pb}(\text{Mg}_{1/3}\text{Nb}_{2/3})\text{O}_3$ - 0.25PbTiO_3
230 transparent ceramic by two - stage sintering. *J. Am. Ceram. Soc.* **93**, 2128–2131 (2010).
- 231 17. Glazer, A., Lewis, J. & Kaminsky, W. An automatic optical imaging system for birefringent
232 media. *Proc. R. Soc. London Ser. A*, **452**, 2751–2765 (1996).
- 233 18. Shvartsman, V. & Kholkin, A. Domain structure of $0.8\text{Pb}(\text{Mg}_{1/3}\text{Nb}_{2/3})\text{O}_3$ - 0.2PbTiO_3 studied by
234 piezoresponse force microscopy. *Phys. Rev. B* **69**, 014102 (2004).
- 235 19. Bai, F., Li, J. & Viehland, D. Domain hierarchy in annealed (001)-oriented $\text{Pb}(\text{Mg}_{1/3}\text{Nb}_{2/3})\text{O}_3$ -x%
236 PbTiO_3 single crystals. *Appl. Phys. Lett.* **85**, 2313–2315 (2004).
- 237 20. Sato, Y., Hirayama, T. & Ikuhara, Y. Real-time direct observations of polarization reversal in a
238 piezoelectric crystal: $\text{Pb}(\text{Mg}_{1/3}\text{Nb}_{2/3})\text{O}_3$ - PbTiO_3 studied via in situ electrical biasing transmission
239 electron microscopy. *Phys. Rev. Lett.* **107**, 187601 (2011).
- 240 21. Kleemann, W. Relaxor ferroelectrics: cluster glass ground state via random fields and random
241 bonds. *Phys. Status Solidi B* **251**, 1993–2002 (2014).
- 242 22. Bokov, A. A., & Ye, Z. G. Recent progress in relaxor ferroelectrics with perovskite structure. *J.*
243 *Mater. Sci.* **41**, 31–52 (2006).
- 244 23. Krogstad, M. J. *et al.* The relation of local order to material properties in relaxor ferroelectrics.
245 *Nat. Mater.* **17**, 718 (2018).
- 246 24. Takenaka, H., Grinberg, I., Liu, S. & Rappe, A. M. Slush-like polar structures in single-crystal
247 relaxors. *Nature* **546**, 391–395 (2017).
- 248 25. Wan, X. M., Luo, H. S., Wang, J., Chan, H. L. W. & Choy, C. L. Investigation on optical
249 transmission spectra of $(1-x)\text{Pb}(\text{Mg}_{1/3}\text{Nb}_{2/3})\text{O}_3$ - $x\text{PbTiO}_3$ single crystals. *Solid State Commun.* **129**,
250 401–405 (2004).
- 251 26. Wemple, S. Polarization fluctuations and the optical-absorption edge in BaTiO_3 . *Phys. Rev. B* **2**,
252 2679 (1970).
- 253 27. Ogawa, T., Matsushita, M. & Tachi, Y. Domain controlled piezoelectric single crystal and
254 fabrication method therefor. *U.S. patent* 2003/0178914 A1(2003).
- 255 28. Yamashita, Y., Yamamoto, N., Hosono, Y. & Itsumi, K. Piezoelectric transducer, ultrasonic
256 probe, and piezoelectric transducer manufacturing method. *U.S. patent* 2015/0372219 A1 (2015).
- 257 29. Chang, W. Y. *et al.* Dielectric and piezoelectric properties of $0.7\text{Pb}(\text{Mg}_{1/3}\text{Nb}_{2/3})\text{O}_3$ - 0.3PbTiO_3
258 single crystal poled using alternating current. *Mater. Res. Lett.* **6**, 537–544 (2018).
- 259 30. Xu, J. *et al.* Piezoelectric performance enhancement of $\text{Pb}(\text{Mg}_{1/3}\text{Nb}_{2/3})\text{O}_3$ - 0.25PbTiO_3 crystals by
260 alternating current polarization for ultrasonic transducer. *Appl. Phys. Lett.* **112**, 182901 (2018).
- 261 31. Budimir, M., Damjanovic, D., & Setter, N. Piezoelectric response and free-energy instability in
262 the perovskite crystals BaTiO_3 , PbTiO_3 , and $\text{Pb}(\text{Zr,Ti})\text{O}_3$. *Phys. Rev. B* **73**, 174106 (2006).

32. Sluka, T., Tagantsev, A. K., Damjanovic, D., Gureev, M., & Setter, N. Enhanced electromechanical response of ferroelectrics due to charged domain walls. *Nat. commun.* **3**, 748 (2012).
33. Xiang, Y., Zhang, R. & Cao, W. Optimization of piezoelectric properties for [001]_c poled 0.94 Pb (Zn_{1/3}Nb_{2/3})O₃–0.06 PbTiO₃ single crystals. *Appl. Phys. Lett.* **96**, 092902 (2010).

Acknowledgements

F.L. and Z.X. acknowledge the support of the National Natural Science Foundation of China (Grant Nos. 51922083, 51831010 and 51761145024) and the 111 Project (B14040). B.W. and L.Q.C. acknowledge the support of the US National Science Foundation under the grant number DMR-1744213 and Materials Research Science and Engineering Center (MRSEC) grant number DMR-1420620. N.Z. thanks the support from NSFC No. 61604123. The computer simulations were performed on the ICS-ACI Computing Systems at Pennsylvania State University through the Penn State Institute for Cyber Science and at the Extreme Science and Engineering Discovery Environment (XSEDE) cluster supported by National Science Foundation grant number ACI-1548562, and specifically, it used the Bridges system, which is supported by NSF award number ACI-1445606 at the Pittsburgh Supercomputing Centre (PSC) under the allocation DMR170006. S.Z. is thankful for the support of ONRG (N62909-18-12168) and ARC (FT140100698). T.R.S. thanks the support of US ONR.

Author Contributions

The work was conceived and designed by S.Z., L.Q.C., and F.L.; C.Q. performed the piezoelectric and optical experiments; F.L. and Z.X. supervised the piezoelectric and dielectric measurements; N.Z. and F.L. supervised the optical experiments; B.W. performed the phase-field simulations and discussed with F.L.; L.Q.C. supervised the simulation work; J.L. assisted piezoelectric measurements; N.Z. and D.W. performed XRD experiments; Y.W. and H.T. assisted the optical measurements; F.L. drafted the manuscript; S.Z., N.Z., L.Q.C. and T.R.S. revised the manuscript; and all authors discussed the results. The authors declare no competing financial interests.

Additional Information

Reprints and permissions information is available at www.nature.com/reprints.

293 Main Figure Legends

294 **Figure 1 Phase-field simulations of the domain structures and evolution of [001]-oriented**
295 **rhombohedral PMN-28PT single crystals via DC and AC poling. a,** Domain structures for unpoled,
296 *DC*-poled and *AC*-poled samples. The black and white vectors on the right show the polarization
297 directions, where the colour denotes the positive (white) and negative (black) polarization components
298 along the [100] direction, respectively. The colours represent different ferroelectric domains, where the
299 corresponding polar directions are illustrated on the right of the figure. Examples of 71° and 109°
300 domain walls are indicated by the red arrows. A beam of light is schematically illustrated in the *DC*-
301 and *AC*-poled cases, indicating that the light may not be scattered as it travels through the *AC*-poled
302 sample. **b,** Snapshots of the domain pattern evolution during the reversal of polarization under *AC*
303 poling. The initial state (i.e., $E = 0.0 \text{ kV cm}^{-1}$) is the *DC*-poled sample. The dimensions of all the
304 domain structure plots are $512 \text{ nm} \times 512 \text{ nm}$. The **videos** illustrating the domain evolution under an *AC*
305 electric field are shown in SI **Videos** 1&2. For comparison, a **video** illustrating the domain evolution
306 under a *DC* electric field is shown in SI **Video** 3.

307 **Figure 2 Analysis of the domain structures for the [001]-oriented PMN-28PT crystals. a,**
308 Birefringence imaging microscopy (BIM), where the colours indicate the orientations (ϕ) of the
309 projection of the principal optical axis on the (001) plane. The red and blue colours represent the
310 projection of the principal axis of the optical indicatrix along the face diagonals on the (001) plane, i.e.,
311 orientation angles ϕ of 45° and 135°, respectively. For example, the projections of the principal axis of
312 the optical indicatrix of the $[\bar{1}\bar{1}1]$ and $[1\bar{1}1]$ domains are illustrated in the schematics on the right of
313 the figure. **b,** Reciprocal space maps of the {222} reflections from differently treated samples measured
314 with high-resolution single-crystal XRD. The colour bars on the right of the figure indicate the intensity
315 of the diffractions. The thickness of the samples is 175 μm .

316 **Figure 3 Comparison of the properties for AC-poled and conventional DC-poled [001]-oriented**
317 **PMN-28PT crystals. a,** Photo of *AC*-poled and *DC*-poled PMN-28PT crystals. The thicknesses of the
318 crystals are 0.5 mm and 1.8 mm, respectively. **b,** Light transmittance of the *AC*-poled and *DC*-poled
319 PMN-28PT crystals. **c,** Piezoelectric coefficient d_{33} and birefringence of the *AC*-poled and *DC*-poled
320 PMN-28PT crystals. Ten *AC*-poled and ten *DC*-poled samples are used for the characterization of
321 piezoelectric coefficient d_{33} , while birefringence is determined from seven points of the *AC*-poled and
322 *DC*-poled samples. The error bars in Fig. 3c present the standard deviations (SD) of the corresponding
323 data.

324 **Figure 4 Phase-field simulations of the domain size effect on the polarization, free energy density**
325 **and properties of the PMN-28PT crystal. a,** a 2D schematic of an [001]-poled PMN-28PT with
326 different 71° domain width (D_{71}). $D_{71}=\text{inf.}$ means there are no 71° domain walls in the system. The
327 polar directions for different colors are depicted on the right of the figure. **b,** Schematic of polar vectors
328 around a 71° domain wall as marked by the green line in Fig. a. The colours represent the angles
329 (deg.=degree) between each polar vector and the [011] direction. The 71° domain width in this
330 schematic is 64 nm. **c,** The averaged magnitude of the spontaneous polarization components P_x ([100]),
331 P_y ([010]) and P_z ([001]) of a ferroelectric domain as a function of the 71° domain width. **d,** The
332 averaged free energy density of the system with respect to the variation of polarization P_z . The free
333 energy density at the stable state (i.e., $\Delta P=0$) is selected as the reference in this figure. **e,** Dielectric
334 permittivity as a function of 71° domain width. **f,** Piezoelectric coefficient as a function of 71° domain
335 width.

338 **Methods**

339 **Sample preparation**

340 To achieve high transparency of rhombohedral PMN-PT crystals, we choose crystal compositions to
341 avoid the presence of multiple phases, e.g., a mixture of rhombohedral, monoclinic, and orthorhombic
342 phases within a MPB region. In particular, we selected the 28%PT composition to stay away from the
343 MPB region (around 33%PT). The PMN-28PT single crystals were grown by a modified Bridgman
344 method at Xi'an Jiaotong University. The crystals were oriented by an X-ray diffraction method with
345 the x , y and z axes along the [100], [010] and [001] directions, respectively, and then cut into the
346 required dimensions for different experiments. The thickness of the samples for the domain observation
347 and birefringence measurement was 0.175 mm. For the other experiments, the thickness of the samples
348 was in the range of 0.5 mm to 4 mm. Vacuum-sputtered gold was applied to both (001) faces of the
349 samples as electrodes.

350 The *AC* and *DC* poling experiments were performed by using a ferroelectric test system (TF Analyzer
351 2000E, aixACCT) with a high-voltage amplifier (TREK 610E). The samples were immersed in silicone
352 oil during the poling process. For *AC* poling, a bipolar triangle wave was applied to the samples with a
353 frequency of $0.1\sim 10^2$ Hz, a cycle number of 5~20, an amplitude of 5 kV cm^{-1} and a poling temperature
354 of $20\sim 60^\circ\text{C}$ ³⁴. We discovered that essentially all the 71° domain walls could be effectively eliminated
355 by using *AC* electric fields with a broad range of frequencies from 0.1 to 100 Hz (see Extended Data
356 Fig. 8). The cycle number was selected to be larger than 10, since the enhancement of dielectric
357 permittivity was found to saturate after 10 cycles, as shown in Extended Data Fig. 9. To minimize the
358 fluctuation of dielectric and piezoelectric properties among different samples, the frequency of AC
359 electric field was selected to be below 10 Hz in this work, as shown Extended Data Fig. 9. To avoid the
360 influence of internal stresses generated during polishing and sputtering of PMN-28PT crystals, a
361 thermal annealing process was applied to the PMN-28PT crystals before AC-poling³⁴. Specifically, the
362 samples were first annealed at 300°C for 5 h and then slowly cooled down to room temperature. The
363 samples then dwelled at room temperature for 5-7 days until the dielectric loss was reduced from 4~5%
364 right after the annealing to around 2%. For *DC*-poling, a conventional poling process of PMN-PT
365 crystals was adopted with a DC electric field amplitude of 5 kV cm^{-1} and a dwelling time of 5 min.

366 For the optical and XRD experiments, the gold electrodes were removed by a solution of potassium
367 iodide and iodine (the mass ratio of KI, I_2 and H_2O was 4:1:40) without affecting the polarization. The
368 (001) surfaces were then carefully polished to optical quality using diamond polishing paste decreasing
369 the average grit size down to $0.05\text{ }\mu\text{m}$. In the electro-optic measurements, a thin layer of gold film (~ 15
370 nm) was deposited on the polished surfaces as electrodes. Silver leads were attached by conductive
371 epoxy to apply a voltage.

372 Here, we would like to note that there are two technical issues associated with the idea using crystals
373 poled along the [111] direction and then cut along the [001] direction to achieve both high piezoelectric
374 coefficient d_{33} and light transparency rather than AC-poling employed in this work.

375 (1) The limitation of crystal size and difficulty to achieve a single domain state by poling [111]
376 oriented rhombohedral crystals: For example, if one needs a [001]-oriented crystal plate with the size of
377 $20\text{mm}\times 20\text{mm}\times 1\text{mm}$ (for medical transducers, practical size of piezoelectric materials is in the range of
378 $20 - 60\text{ mm}$), one first needs a [111]-oriented crystal with the size of $\sim 30\times 30\times 30\text{ mm}$. To pole a crystal
379 with the thickness of 30 mm along its spontaneous polarization direction is almost an impossible task
380 due to the severe cracking as a result of the internal stress development during poling³⁵. In addition,
381 one cannot guarantee the composition homogeneity for the [001]-oriented crystal plates made by this
382 process because of the composition segregation along the crystal growth direction of Bridgman grown
383 PMN-PT crystal boules.

(2) The instability of a single domain state and the issue of depolarization: Preparing the [111]-poled samples with rotated d_{33} involves high-temperature processes, such as attaching a crystal onto a sample holder for cutting, heat generation during cutting, and sputtering transparent electrodes (the temperature for sputtering of ITO electrodes is 300°C~600°C). One may argue that we can adopt careful low temperature processes and utilize low temperature transparent electrodes (e.g., silver nanowires) to prepare the samples. However, based on our experiences, this is really a difficult task, as we need to use special binders and sample holders and drastically slow down the cutting speed of the cutting machine; meanwhile, the adhesion of electrodes will be greatly affected by using silver nanowires to replace ITO. Even by using all these precautions and approaches, the samples are still likely to be depolarized to some extent because of the instability of a single domain state. In addition, the [001]-oriented samples made by this process cannot be re-poled if they are de-poled accidentally. This is due to the fact that we cannot recover the original [111]-oriented samples.

Dielectric and piezoelectric measurements

The piezoelectric coefficients were determined by a combination of a quasi-static d_{33} metre (ZJ-6A) and an electric-field-induced strain measurement. The electric-field-induced strain was measured by a ferroelectric test system (TF Analyzer 2000E, aixACCT, Germany) with a laser interferometer (SIOS SP-S 120E, Germany). The dielectric permittivity was measured using an LCR metre (E4980A, KEYSIGHT technologies, CA, USA). In the measurements of temperature-dependent properties, the piezoelectric coefficient d_{33} and electromechanical coupling factor k_{33} of PMN-PT crystals are determined by the resonance method according to IEEE Standard.

Optical transmittance measurement

Transmission spectra were measured by a UV–VIS–IR spectrophotometer (JASCO V–570, Japan) at wavelengths ranging from 300 to 2500 nm. The incident light was set to transmit through the crystal along the poling direction, which was perpendicular to the (001) surface.

According to the Fresnel equations, the reflection loss at two faces of the crystal plate was calculated from 450 to 850 nm through,

$$R = \frac{(n-1)^2}{n^2+1} \quad (1)$$

where n is the wavelength-dependent index of refraction, calculated from the Sellmeier equation for a PMN-28PT single crystal given in Refs. 36&37.

The effective loss coefficient α_{eff} , a combination of the scattering coefficient κ and the absorption coefficient, α ($\alpha_{eff} = \kappa + \alpha$), was calculated using the transmission data from samples of different thicknesses,

$$\alpha_{eff} = -\frac{\ln(T_2/T_1)}{t_2-t_1} \quad (2)$$

where T_1 and T_2 are the transmittances of the two samples with thicknesses t_1 and t_2 , respectively.

Domain characterizations by optical methods

Polarized light microscope (PLM). The domain patterns and their extinction behaviours were observed using a PLM with a 0°/90° crossed polarizer/analyser (P/A) pair (OLYMPUS BX51, Japan). The optical retardation was measured using a thick Berek compensator (OLYMPUS U-CTB ranging from 0~10 λ) and an interference filter (IF546, λ =546.1 nm). The birefringence was calculated as the ratio of the retardation to the sample thickness. In the following, we would like to explain the cancellation

effect of birefringence as light travels across a 71° domain wall. For a single domain rhombohedral ferroelectric, the parameters n_o and n_e are the refractive indices for the ordinary light and extraordinary light propagating along z-axis, respectively. The parameters Δn_1 and Δn_2 are the birefractive indices of two different domains on both sides of a 71° domain wall. Since the principal axes of the optical indicatrices of the domains on both sides of a 71° domain wall (e.g., the domains with polar vectors along [111] and $[\bar{1}\bar{1}1]$ directions) are perpendicular to each other on the (001) plane, the relation between Δn_1 and Δn_2 is: $\Delta n_1 = -\Delta n_2$. Thus as the light travels across a 71° domain wall, the measured birefringence can be expressed by the following equation:

$$\Delta n^* = \frac{\Delta L}{d} = \frac{\Delta n_1 \cdot d_1 + \Delta n_2 \cdot d_2}{d_1 + d_2} = \Delta n_1 \cdot \frac{d_1 - d_2}{d} \quad (3)$$

where d_1 and d_2 are the lengths of optical path within the [111] and $[\bar{1}\bar{1}1]$ domains, respectively, ΔL is the optical retardation caused by birefringence, and d is a sum of d_1 and d_2 . It is obvious that the measured birefringence will be quite small if the values of d_1 and d_2 are similar.

Birefringence imaging microscopy (BIM). The domain orientation measurements were performed using BIM equipment (Metropol, Oxford Cryosystems, UK). Monochromatic light with a wavelength of 590 nm was used as the light source. A quarter-wave plate and a polaroid (P_2) were placed at a 45° position to produce circularly polarized light. The circularly polarized light was converted to elliptical polarization after passing through an optically anisotropic specimen. The light then transmits through a linear analyser (P_2) rotating about the microscope axis at a frequency of ω . Finally, the intensity measured by the charge-coupled device (CCD) camera as a function of ω is given by

$$I = \frac{1}{2} I_0 [1 + \sin 2(\omega t - \varphi) \sin \delta] \quad (4)$$

where t is time, φ is the angle between the horizontal direction and the principal axis of the optical indicatrix, δ is the phase shift introduced to the light rays passing through the anisotropic sample with a certain thickness, and I_0 is the intensity of the unpolarized light. After rotating the analyser 10 times, it is possible to obtain the intensity of each pixel on the recorded image, refine the I_0 , $|\sin \delta|$, and φ values, and construct the false-colour images.

High-resolution X-ray diffraction experiments

High-resolution single-crystal XRD experiments were carried out to analyse the {222} Bragg reflections for (001)-oriented PMN-PT crystals. A high-resolution diffractometer (PANalytical X'Pert Pro MRD), equipped with $\text{CuK}\alpha_1$ radiation, a hybrid mirror monochromator, an open Eulerian cradle and a solid-state PIXcel detector, was used for a precise two-dimensional 2θ - ω scan of the {222} Bragg peaks. The reciprocal space maps were collected with step sizes of 0.004° in ω and 0.004° in 2θ . The intensity of the patterns was accumulated along the ω or 2θ direction and then fitted to the pseudo-Voigt function:

$$f(x) = a_1 \left\{ a_4 \cdot \frac{1}{1 + \left(\frac{x - a_2}{a_3} \right)^2} + (1 - a_4) \exp \left[- \left(\frac{x - a_2}{a_3} \right)^2 \right] \right\} \quad (5)$$

where a_1 is the intensity of the peak, a_2 is the position of the peak, a_4 is the mixing parameter of the Gaussian and Lorentzian profiles, and a_3 is proportional to the FWHM, which can be calculated using the equation,

$$\text{FWHM} = 2\sqrt{\ln 2} \cdot a_3 \quad (6)$$

Electro-optic measurements

The electro-optic (E-O) coefficients of the samples were measured using a modified Mach-Zehnder interferometer. The light source was a 632.8 nm He-Ne laser. For the longitudinal mode, the light beam and the applied electric field were both parallel to the poling direction. In this mode, the longitudinal effective linear E-O coefficient (γ_c^{L*}) was measured.

For the transverse mode, the light beam travels along the [110] direction, and the electric field was applied along the [001] poling direction of the sample. The linear E-O coefficients γ_{13}^* and γ_{33}^* were measured when the polarization directions of the laser beam were perpendicular and parallel to the poling direction, respectively. The transverse effective linear E-O coefficient (γ_c^{T*}) was calculated by the equation:

$$\gamma_c^{T*} = \gamma_{33}^* - n_o^3 \gamma_{13}^* / n_e^3 \quad (7)$$

where n_o and n_e are the refractive indices of the ordinary and extraordinary light, respectively. The refractive indices were calculated from the data of mono-domain crystals^{36,37}. The marker (*) indicates that the measured E-O coefficient is a combination of the inverse piezoelectric effect and the intrinsic E-O effect.

Phase-field simulations

The domain evolution and piezoelectric responses were obtained by performing phase-field simulations. A domain structure is described by the spatial distribution of the ferroelectric polarization \mathbf{P} . The temporal evolution of the polarization and thus the domain structure is described by the time-dependent Ginzburgh-Landau (TDGL) equation:

$$\frac{\partial \mathbf{P}}{\partial t} = -L \frac{F(\mathbf{P})}{\delta \mathbf{P}} \quad (8)$$

where t is time, F is the total free energy, and L is the kinetic coefficient. The total free energy contains contributions from the bulk, elastic, electric, and gradient energies. Details of using the phase-field method to simulate the switching behaviours of ferroelectric single crystals can be found in Ref. 38&39. The Landau coefficients were adapted from Ref. 40 using the experimental ferroelectric, piezoelectric, and dielectric properties of PMN-28PT crystals at room temperature⁴⁰. Based on this thermodynamic potential, the calculated equilibrium phase is rhombohedral at room temperature with a spontaneous polarization of $\sim 0.38 \text{ C m}^{-2}$, a relative dielectric constant of ~ 5500 along [001], and a longitudinal piezoelectric coefficient $\sim 1850 \text{ pC N}^{-1}$ along [001], which are in reasonable agreement with our experiments. The electrostrictive coefficients measured by Li *et al.*⁴¹ for PMN-28PT were adopted. The gradient energy coefficients were assumed to be isotropic, and the domain wall width was assumed to be approximately $\sim 2 \text{ nm}$. It should be noted here that the Landau potential used in this work represents the averaged free energy of a single-domain PMN-28PT crystal, which incorporates the impacts of the nanoscale heterogeneous polar regions (several nanometres) in the free energy and electromechanical properties⁴².

To simulate the AC and DC poling processes, we first obtained an unpoled domain structure from a random noise distribution of the polarization within a quasi-2D grid with $512 \Delta x \times 512 \Delta x \times 1 \Delta x$ grid points ($\Delta x = 1 \text{ nm}$). Then, a low-frequency triangle wave was applied to mimic the AC poling, whereas a single-step square wave was used to represent the DC poling. The magnitude of the poling electric field was 10 kV cm^{-1} . We performed phase field simulations at different mechanical boundary conditions, i.e., the stress-free condition which assumes the averaged stress of the simulated system equal to zero, and the clamped condition which assumes the averaged strain equal to zero. Fig. 1 shows the simulated results for the clamped condition, and the simulation results at stress-free condition are presented in Extended Data Fig. 3b. The practical condition in experiments is likely between these two extreme mechanical conditions. The conclusion that the sizes of 71° domains in AC-poled samples are

always much larger than the DC-poled ones holds for both mechanical boundary conditions while the 109° domain layer thickness is similar in AC- and DC-poled samples. It is interesting to note that the AC-poling can lead to completely layered 109° domain structure without 71° domain walls under the stress-free condition.

The dielectric permittivity ϵ_{33} and piezoelectric coefficient d_{33} were obtained by evaluating the variations of polarization and longitudinal strain under a small electric field of 0.5 kV cm⁻¹ along the [001] direction. We also calculate the free energy by applying small test electric fields (E_z is from 0 to 1 kV cm⁻¹, which is sufficient small without causing domain wall motion or phase transition) and plot the averaged free energy density as a function of the change of overall the polarization P_z along the poling direction.

The computer simulations were performed on the ICS-ACI Computing Systems at Pennsylvania State University and at the Extreme Science and Engineering Discovery Environment (XSEDE) cluster, which is used the Bridges system at the Pittsburgh Supercomputing Center (PSC)^{43,44}.

Method references

34. Li, F., Qiu, C.R., Xu, Z., Chen, L.Q., Wang B., Zhang, S.J. & Shrout T.R. Transparent ferroelectric crystals with ultrahigh piezoelectricity. Provisional U.S. Patent 16/541,309 (2019).
35. Li, F., Wang, L., Jin, L., Xu, Z., and Zhang S.J. Achieving single domain relaxor-PT crystals by high temperature poling. *CrystEngComm* **16**, 2892–2897 (2014)
36. Wan, X. M., Chan, H. L. W., Choy, C. L., Zhao, X. & Luo, H. Optical properties of (1-x)Pb(Mg_{1/3}Nb_{2/3})O₃-xPbTiO₃ single crystals studied by spectroscopic ellipsometry. *J. Appl. Phys.* **96**, 1387–1391 (2004).
37. Wan, X. M. *et al.* Refractive indices and linear electro-optic properties of (1-x)Pb(Mg_{1/3}Nb_{2/3})O₃-xPbTiO₃ single crystals. *Appl. Phys. Lett.* **85**, 5233–5235, (2004).
38. Wang, J., Shi, S. Q., Chen, L.-Q., Li, Y. & Zhang, T. Y. Phase-field simulations of ferroelectric/ferroelastic polarization switching. *Acta. Mater.* **52**, 749–764 (2004).
39. Wang, J., Wang, B. & Chen, L.-Q., Understanding, predicting, and designing ferroelectric domain structures and switching guided by the phase-field method. *Annu. Rev. Mater. Res.* **49**, 6.1–6.26 (2019).
40. Khakpash, N., Khassaf, H., Rossetti Jr, G. A. & Alpay, S. P., Misfit strain phase diagrams of epitaxial PMN-PT films. *Appl. Phys. Lett.* **106**, 082905 (2015).
41. Li, F., Jin, L., Xu, Z., Wang, D., & Zhang, S. J. Electrostrictive effect in Pb(Mg_{1/3}Nb_{2/3})O₃-xPbTiO₃ crystals. *Appl. Phys. Lett.*, **102**,152910 (2013).
42. Li, F. *et al.* The origin of ultrahigh piezoelectricity in relaxor-ferroelectric solid solution crystals. *Nat. Commun.* **7**, 13807 (2016).
43. Towns, J. *et al.* XSEDE: Accelerating Scientific Discovery. *Computing in Science & Engineering*. **16**, 62-74 (2014).
44. Nystrom, N. A., Levine, M. J., Roskies, R. Z., & Scott, J. R. 2015. Bridges: A Uniquely Flexible HPC Resource for New Communities and Data Analytics. In *Proceedings of the 2015 Annual Conference on Extreme Science and Engineering Discovery Environment* (St. Louis, MO, July 26-30, 2015). XSEDE15. ACM, New York, NY, US.

550

551 **Data Availability Statement**

552 The data that support the findings of this study are available upon request by contacting the
553 corresponding authors.

554 **Code availability**

555 The phase-field simulations are performed using the commercial Mu-PRO software package which is
556 available from Mu-PRO LLC, State College, PA, 16803 USA (<http://mupro.co/contact/>).

557

558 **Extended Data Figure Legends**

559 **Extended Data Figure 1 | Schematic diagrams of the projections of optical indicatrices on both**
560 **sides of a domain wall. a**, 109°-domain wall; **b**, 71°-domain wall. The prerequisite of the light
561 scattering and reflection at an interface is the difference of refractive indices between the optical media
562 on each side of the interface. As shown here, the principal axes of the optical indicatrix projected on the
563 (001) planes are the same for domains on each side of a 109° domain wall. Thus, the refractive indices
564 n_o and n_e do not change as the light goes across a 109° domain wall, resulting in the absence of light
565 scattering and/or reflection. In contrast, the principal axis of the optical indicatrix projected on the (001)
566 plane rotates by 90° as the light travels across a 71° domain wall, resulting in the alternating of
567 refractive indices n_o and n_e . This is the reason that 71° domain walls scatter and/or reflect the light.

568 **Extended Data Figure 2 | The variation of various energies of PMN-28PT during the first four**
569 **cycles of AC-poling.** The data are obtained by phase-field simulations. Here we plot the normalized
570 energies that are dimensionless.

571 **Extended Data Figure 3 | Effects of system size and mechanical boundary conditions on the AC-**
572 **and DC-poled domain structures from phase-field simulations. a**, Effects of system size (at the
573 clamped boundary condition). **b**, Effects of mechanical boundary condition (the scale of the simulation
574 is 512×512 nm).

575 **Extended Data Figure 4 | Characterization of the domain size along the poling direction for**
576 **[001]-oriented rhombohedral relaxor-PT crystals. a**, PLM images on the (100) face for [001]-poled
577 PMN-28PT crystals by AC poling. **b**, PLM images on the (100) face for [001]-poled PMN-28PT
578 crystals by DC poling. **c**, Distribution of the thickness of laminar domains for AC-poled sample
579 measured from Fig. **a**. **d**, Distribution of the thickness of laminar domains for DC-poled sample
580 measured from Fig. **b**. The thickness of the samples is around 100 μm . As shown in these figures, no
581 clear difference is observed for the thickness of laminar domains between AC- and DC-poled samples.

582 **Extended Data Figure 5 | Pseudo-Voight fittings of the {222} diffraction peaks at high-2 θ . a and b**
583 **are for the unpoled sample; c and d are for the DC-poled sample; e and f are for the AC-poled sample;**
584 **a, c, and e**, the intensity of the patterns, accumulated along Ω direction. **b, d and f**, the intensity of the
585 patterns, accumulated along 2 θ direction.

586 **Extended Data Figure 6 | Effective light absorption coefficients of AC- and DC-poled PMN-28PT**
587 **crystals.**

588 **Extended Data Figure 7 | The temperature stability of AC-poled and DC-poled PMN-28PT**
589 **crystals. a**, Piezoelectric coefficient d_{33} , dielectric permittivity $\epsilon_{33}^T/\epsilon_0$ and electromechanical coupling
590 factor k_{33} as a function of temperature. For each testing temperature, the dwelling time is 10 mins. **b**,

591 Domain structure of AC-poled PMN-28PT crystals as a function of temperature. For this experiment,
592 the temperature is increased from 25 to 100°C. The increase rate is 1°C/min. For each testing
593 temperature, the dwelling time is 30 mins. At temperatures below rhombohedral-tetragonal phase
594 transition temperature (~95 °C), the domain structure remains essentially the same and no
595 depolarization behaviour is observed, indicating AC-poled crystals can be used up to their respective
596 phase transition temperatures.

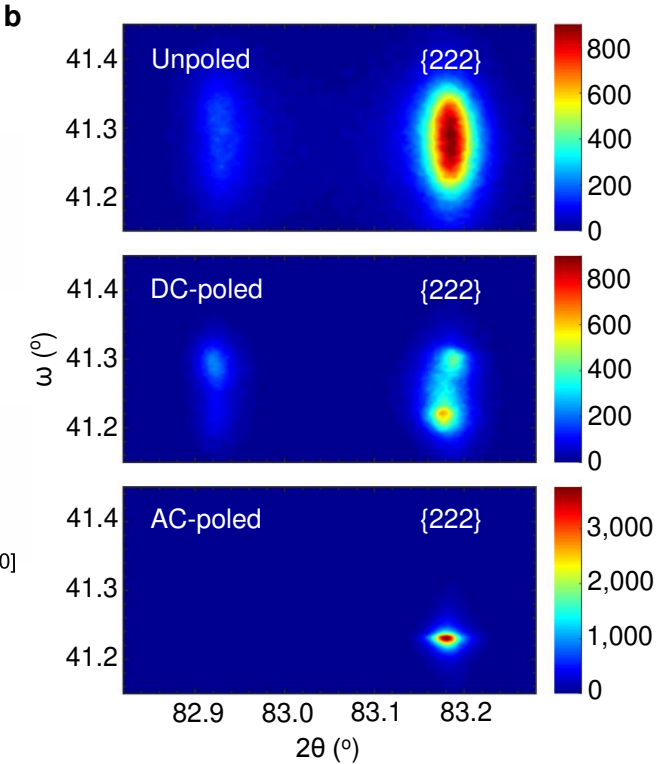
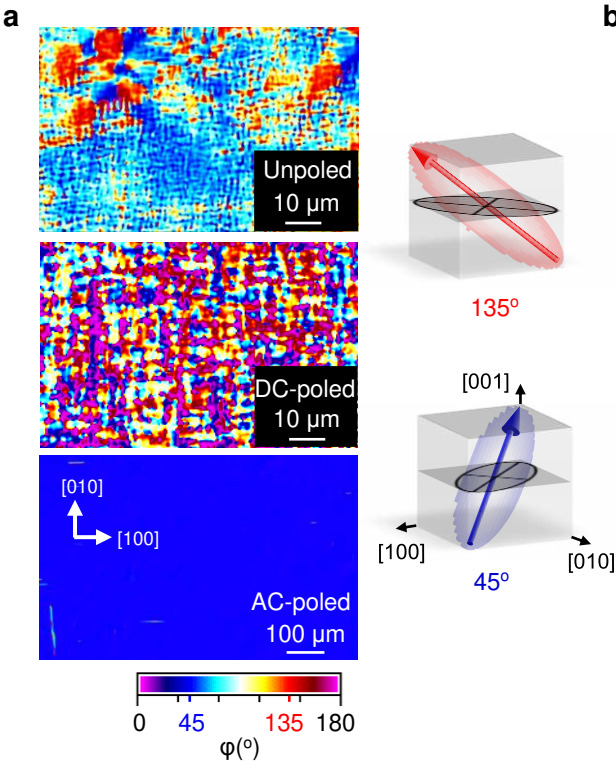
597 **Extended Data Figure 8 | Polarized light microscopic (PLM) images of [001]-oriented PMN-28PT**
598 **crystals with different poling conditions.** Images **a**, **b**, **c**, and **d** are obtained from the crystals poled at
599 frequencies of 0.1 Hz, 1 Hz, 10 Hz and 100 Hz, respectively. Images **e** and **f** are the enlarged ones of
600 the regions of **b** and **c**, respectively. Images **g**, **h** and **i** are obtained from the crystals poled by a DC
601 electric field. The thickness of the samples is 0.5 mm. For DC-poled samples, there are numerous
602 cross-like domain walls while these types of domain walls are removed by an AC electric field. For this
603 experiment, the thickness of the samples is 0.5 mm.

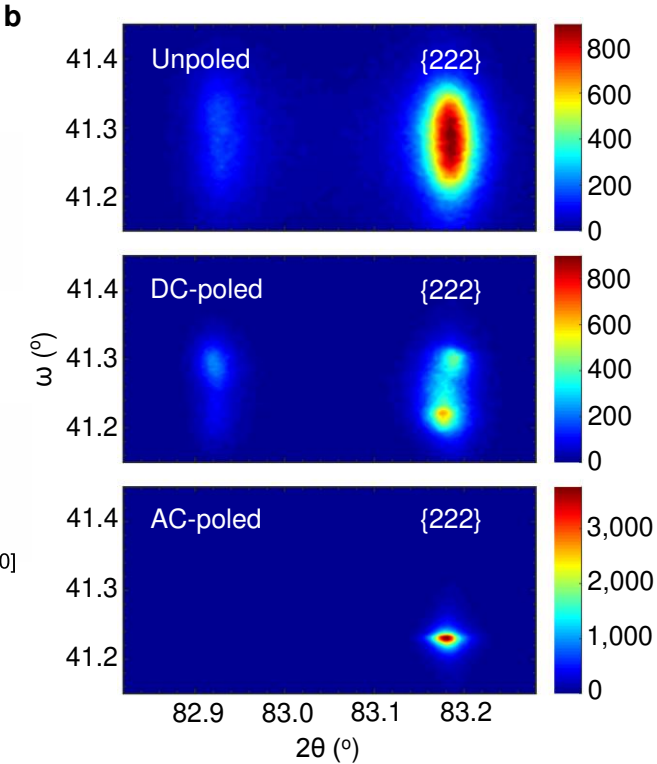
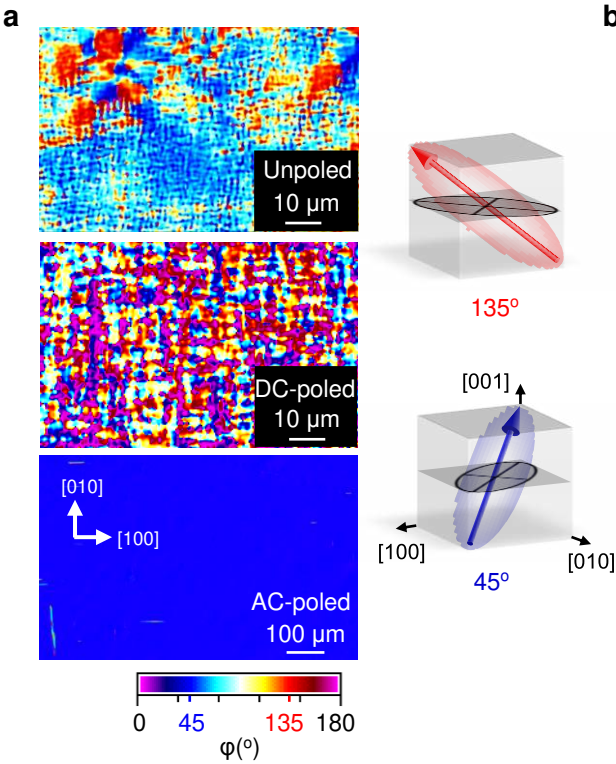
604 **Extended Data Figure 9 | Dielectric permittivity and piezoelectric coefficient of the AC-poled**
605 **PMN-28PT crystal as a function of the cycle number and frequency.** **a**, Dielectric permittivity as a
606 function of the cycle number. **b**, Dielectric permittivity as a function of the frequency. **c**, Piezoelectric
607 coefficient as a function of the frequency. Five samples are used for each frequency. The error bars
608 indicate the standard deviations (SD) of the corresponding data.

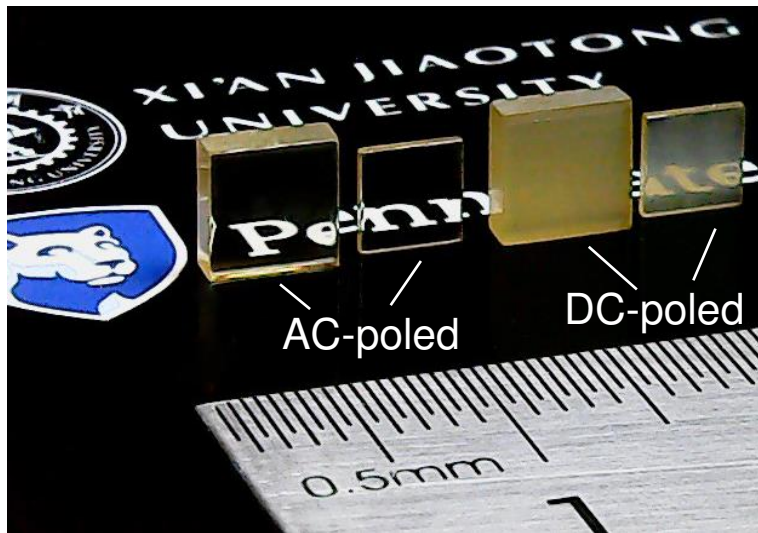
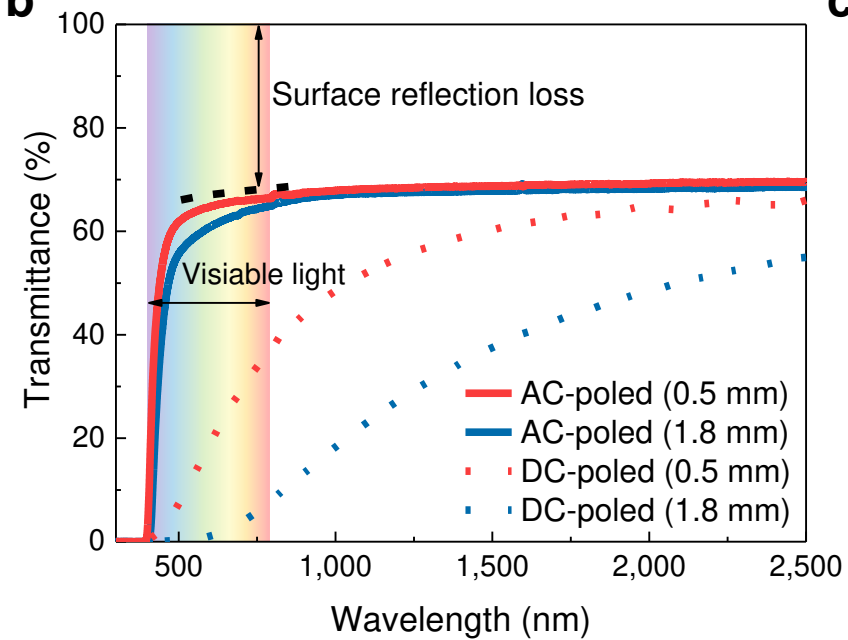
609

610 **Extended Data Table 1 | Electromechanical and electro-optical properties of [001]-oriented**
611 **PMN-28PT crystals via AC- and DC-poling.** To measure coefficient γ_c^{L*} , both the applied electric
612 field and the light beam are along the [001] direction. To measure coefficients γ_{33}^* and γ_{13}^* , the applied
613 electric field is along the [001] direction, and the light beam is along the [110] direction. Note: it is
614 difficult to obtain accurate electro-optical coefficients for DC-poled samples, owing to the strong light
615 scattering by the high density of ferroelectric domain walls. The errors indicate the standard deviations
616 (SD) of the corresponding data (more than five samples/data-points are used for each measurement).

617





a**b****c**